lubricants

MDPI

Article

Oil Film Thickness and Meshing Efficiency for a Novel Closed Movable Tooth Gear Reducer

Shuo Yang and Lizhong Xu *

School of Mechanical Engineering, Yanshan University, Qinhuangdao 066004, China; 23yangshuo@stumail.ysu.edu.cn
* Correspondence: xlz@ysu.edu.cn; Tel.: +86-335-8057031

Abstract: Equations are developed for the relative sliding velocities, entrainment velocities, forces, friction coefficients, effective radius of curvature, oil film thickness, friction loss, and meshing efficiency for a novel closed movable tooth gear reducer. Using these equations, the relative sliding velocities and entrainment velocities of the reducer are studied. The meshing efficiencies and their changes along with meshing positions and main parameters are analyzed. Changes of the meshing efficiencies along with load torque are also studied. An efficiency experiment of the reducer prototype is carried out. Results indicate that the meshing efficiency of the novel closed reducer increases with increasing eccentric distance. When an error in the eccentric distance occurs, the meshing efficiency is significantly reduced. The measured efficiency is close to the calculated one, supporting the theoretical studies.

Keywords: oil film thickness; efficiency; reducer; movable tooth; closed; relative velocities

1. Introduction

With the development of intelligent deformable aircraft, mechanical arms for aerospace, and other related technologies, driving devices must meet higher requirements for miniaturization, intelligence, efficiency, and reliability. The RV (rotating vector) reducer consists of a planetary gear drive and a cycloidal pinwheel drive, which is difficult to miniaturize because of its complex structure [1]. A harmonic gear reducer is widely used in robot joint driving, but it is difficult to realize high transmission accuracy because of deformation of the flexible ring [2,3].

Therefore, it is urgent to explore a new type of miniature joint-driving mechanism for robotic applications. Movable tooth drives are widely considered because of their large speed ratio and simple processing technology [4,5]. In the 1980s–1990s, reducers with sine-tooth profiles were studied, and the single-swing-tooth reducer was optimized [6–8]. In the 21st century, many additional studies have been carried out. A toothless reducer was proposed, and its parameter optimization was completed [9,10]. In addition, the tooth profile of a two-stage cycloid pinwheel reducer was calculated [4,11]. A planetary drive with ball teeth based on axial pre-tightening was investigated, and its nonlinear dynamic performance of transmission was studied [12]. To increase meshing efficiency, a thin movable tooth gear reducer was investigated [13]. To reduce the weight of the reducer and the contact stress, an eccentric movable tooth drive was proposed [14,15]. The transmission error, thermal strain, and thermal stress of a swing-rod movable toothed drive were analyzed [16,17]. Two movable sine-tooth drives were integrated with each other to obtain a two-stage drive with a large speed ratio and small size [18]. In addition, a movable

check for updates

Received: 5 January 2025
Revised: 4 February 2025
Accepted: 5 February 2025
Published: 7 February 2025

Citation: Yang, S.; Xu, L. Oil Film Thickness and Meshing Efficiency for a Novel Closed Movable Tooth Gear Reducer. *Lubricants* **2025**, *13*, 74. https://doi.org/10.3390/lubricants13020074

Copyright: © 2025 by the authors. Licensee MDPI, Basel, Switzerland. This article is an open access article distributed under the terms and conditions of the Creative Commons Attribution (CC BY) license (https://creativecommons.org/licenses/by/4.0/).

tooth drive was combined with other actuators. To reduce the system size, the movable tooth drive was integrated with a piezoelectric motor or electromagnetic actuator to give several integrated drive systems [19,20]. To further reduce the axial size of the reducer, we previously proposed a novel closed two-stage movable tooth gear reducer [21].

Operation efficiency is one of the important performance indices of the reducer. The determination of operation efficiency and studies of its influencing factors are of great significance to the practical application of the reducer. In order to solve the meshing efficiency of this reducer, it is necessary to determine its meshing characteristics, meshing force, friction, and lubrication characteristics.

However, in the working process of the reducer, in some angle ranges, the movable teeth mesh with the inner raceway of the wave generator or center wheel; in other angle ranges, the movable teeth mesh with the outer raceway of the wave generator or center wheel. The meshing pair changes periodically with the rotation angle, which increases the difficulty of solving the problem. No similar research work has been reported in the world.

In this paper, for the novel closed two-stage movable tooth gear reducer, considering that the meshing pair changes periodically with the rotation angle, the meshing characteristics of the reducer are analyzed in detail. Based on this, the equations of the relative sliding velocities and entrainment velocities of the meshing pair are proposed. For different rotation angle ranges, the different equations of the effective radius of curvature, forces, friction coefficients, oil film thickness, and friction loss are deduced. Then, the equations of the meshing efficiency for the reducer are given.

Using the equations given here, the relative sliding velocities and entrainment velocities of the reducer are investigated. Meshing efficiencies and their changes, along with meshing positions and principal parameters, are analyzed. Changes of the meshing efficiencies along with load torque are also studied. An efficiency experiment of the reducer prototype is carried out. It illustrates the studies in this paper. These studies are useful for the load-carrying ability design of the novel reducer.

2. Materials and Methods

2.1. Structure Composition and Working Principle

The structure of the novel closed movable tooth gear reducer is shown in Figure 1. It consists of an input shaft, two center rings (CR1 and CR2), two movable tooth frames (MTF1 and MTF2), and two sets of the movable teeth (MT1 and MT2). In the movable tooth gear reducer, the steel balls are just movable teeth. On the movable tooth frames, there is no tooth. On the input shaft, there are two wave generators (WG1 and WG2), which drive two stages of the drives simultaneously. The reducer is closed by the input shaft. Its left end is an eccentric circular orbit (first-stage WG1), providing input speed for the first-stage drive; its right end is also an eccentric circular orbit (second-stage WG2). The detailed dimensions of the proposed reducer are given in Table 1. The maximum dimension for miniature driving devices is its outer diameter, and it is equal to 70 mm. The steel balls are made of bearing steel (Gr15), and the center wheel, wave generator, and movable tooth frame are made of alloy steel (42CrMo). Here, Z_{G1} and Z_{G2} are the MT numbers for the first- and second-stage drives, and Z_{K1} and Z_{K2} are the sine-wave period numbers of the CR for the first- and second-stage drives; a_1 is the eccentric distance; $b_1 = r_1 + R_1$, where R_1 and r_1 are the radii of WG1 and MT1, respectively; a_2 is the eccentric distance; $b_2 = r_2 + R_2$, where R_2 and r_2 are the radii of WG2 and MT2, respectively; r_1 and r_2 are the radii of the first- and second-stage movable teeth, respectively. In this paper, they are equal to each other: $r_1 = r_2 = r$.

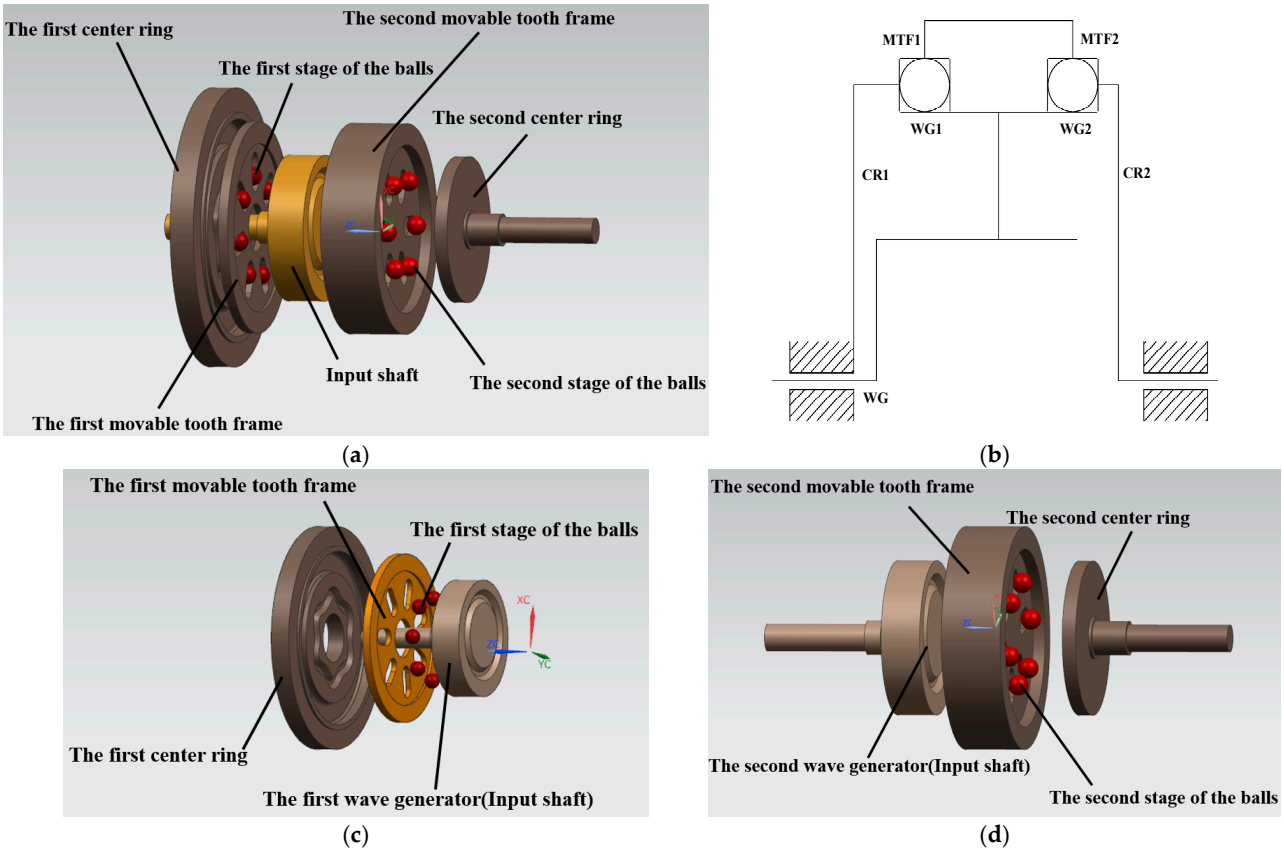


Figure 1. Structure of a closed two-stage movable tooth gear reducer: (**a**) structure of the reducer; (**b**) schematic diagram; (**c**) the first-stage; and (**d**) the second-stage.

Table 1. Calculated parameters.

Z_{K1}	Z_{G1}	Z_{K2}	Z_{G2}	a_1 (mm)	b_1 (mm)	a_2 (mm)	b_2 (mm)	r (mm)
6	7	5	6	1.3	16	1.3	16	6

In the first-stage drive, the eccentric circular orbit of the WG1 is input, center ring CR1 is fixed, and movable tooth frame MTF1 is output. The two MTF1 and MTF2 are attached to each other so that they have the same speed during operation. In the second-stage drive, both eccentric circular orbit of WG2 and the movable tooth frame MTF2 are input, and center ring CR2 is output. The eccentric motion of the first-stage WG1 drives the first-stage steel balls MT1 to run in the slot of the first-stage MTF1 and the track of the first-stage CR1. Since the CR1 is fixed, the first-stage steel balls drive the first-stage MTF1 to rotate about its center. The second MTF2 has the same speed as the first one, as above stated. The second MTF2 and the second WG2 are used as inputs to jointly push the second-stage MT2 steel balls to form differential motion. The second MT2 drives the second CR2 to rotate and to provide power.

The average speed ratio is for the novel closed reducer is [21]

$$i_s = \frac{Z_{K2}Z_{G1}}{Z_{K2}Z_{G1} - Z_{K1}Z_{G2}} \tag{1}$$

2.2. Velocities in Meshing Pairs

In the operation of the reducer, there is relative sliding between the steel balls and their meshing elements. Figure 2a shows the relative velocities in the first-stage drive. Here, φ_{1i} and φ_{2i} are, respectively, the rotation angles of the first-stage WG and MTF; v_{1mk} is

the relative sliding velocity between the first-stage MT and CR; v_{1mg} is the relative sliding velocity between the first-stage MT and MTF; v_{1mh} is the relative sliding velocity between the first-stage MT and WG; $v_{1m\tau}$ is the velocity component of the velocity v_{1mk} in the tangent direction; α_1 is the angle, dependent on slope, of the center curve of the first-stage CR; and $\gamma_1 = \arcsin\left(\frac{a_1}{b_1}\sin(Z_{k1}\varphi_{2i})\right)$. The angle α_1 is given by

$$\alpha_1 = \arctan\left(-\frac{Z_{k1}\sin z_{k1}\varphi_{2i}\cos\varphi_{2i} + \sqrt{\lambda_1^2 - \sin^2 Z_{k1}\varphi_{2i}}\sin\varphi_{2i}}{z_{k1}\sin z_{k1}\varphi_{2i}\sin\varphi_{2i} - \sqrt{\lambda_1^2 - \sin^2 Z_{k1}\varphi_{2i}}\cos\varphi_{2i}}\right)$$

Here, $\lambda_1 = b_1/a_1$ and Z_{k1} is the wave number of CR1.

S_{c1} is the central distance between the first-stage CR and MT, given by

$$S_{c1} = a_1\cos Z_{K1}\varphi_{2i} + \sqrt{b_1^2 - a_1^2\sin^2 Z_{K1}\varphi_{2i}} \tag{2}$$

The velocity v_{1mg} is

$$v_{1mg} = \omega_2 \cdot \frac{dS_{c1}}{d\varphi_{2i}} = -\omega_2\left(Z_{k1}a_1\sin Z_{k1}\varphi_{2i} + \frac{a_1^2 Z_{K1}\sin 2Z_{K1}\varphi_{2i}}{2\sqrt{b_1^2 - a_1^2\sin^2 Z_{K1}\varphi_{2i}}}\right) \tag{3}$$

where ω_2 is the angular speed of the first-stage MTF.

Figure 2e shows meshing details between the MT and other elements. β is the half-angle of the contact arc between the MT and CR or WG.

From Figure 2a,b, the tangent velocity of MT1 along with MTF1 at the outer track of CR1 is

$$v_{1m\tau w} = \omega_2(S_{c1} + r\cos\beta) \tag{4}$$

The tangent velocity of MT1 along with MTF1 at the outer track of the CR1 is

$$v_{1m\tau n} = \omega_2(S_{c1} - r\cos\beta) \tag{5}$$

Thus, the relative sliding velocity between the first-stage MT and the outer track of CR1 is

$$v_{1mkw} = \sqrt{v_{1m\tau w}^2 + v_{1mg}^2} \tag{6}$$

The relative sliding velocity between the first-stage MT and the inner track of CR1 is

$$v_{1mkn} = \sqrt{v_{1m\tau n}^2 + v_{1mg}^2} \tag{7}$$

The relative sliding velocity between the first-stage MT and the outer track of WG1 is

$$v_{1mhw} = v_{1m\tau w} - \omega_1(S_{c1} + r\cos\beta)\cos(\varphi_{2i} - \alpha_1) \tag{8}$$

The relative sliding velocity between the first-stage MT and the inner track of WG1 is

$$v_{1mhn} = v_{1m\tau n} - \omega_1(S_{c1} - r\cos\beta)\cos(\varphi_{2i} - \alpha_1) \tag{9}$$

where ω_1 is the angular speed of the first-stage WG.

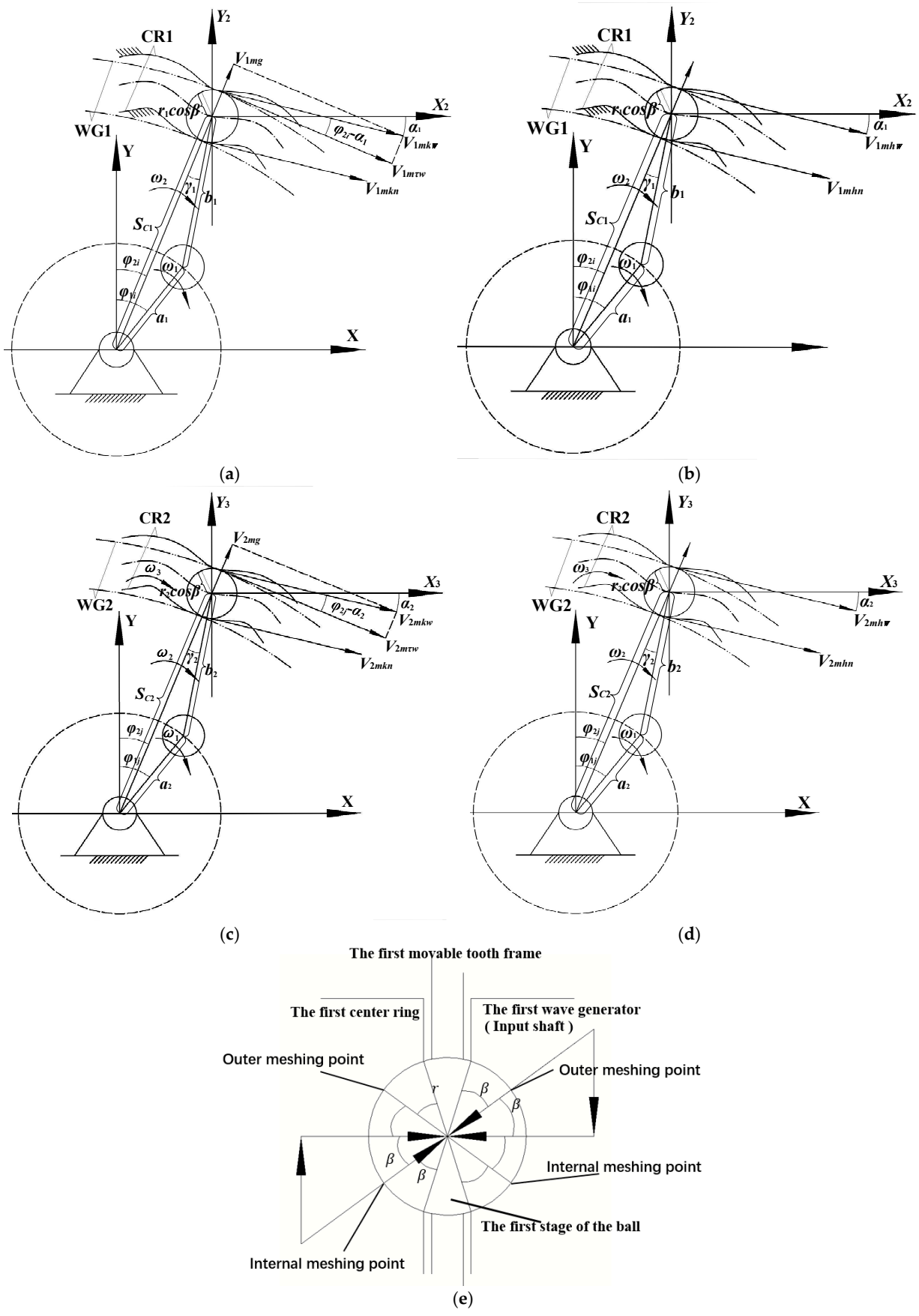


Figure 2. Relative velocities and meshing details in the drive: (**a**) relative velocities (stage 1: MT1 and CR1); (**b**) relative velocities (stage 1: MT1 and WG1); (**c**) relative velocities (stage 2: MT2 and CR2); (**d**) relative velocities (stage 2: MT2 and WG2); and (**e**) meshing details.

Similarly, velocities in the second-stage drive are shown in Figure 2c,d. Here, the second center ring is moving, unlike for the first-stage drive. Here, ω_3 is the angular velocity of the second-stage CR.

The tangent velocity of the second-stage MT at the inner track of the CR is

$$v_{2m\tau n} = \omega_2(S_{c2} - r\cos\beta) \tag{10}$$

The tangent velocity of the second-stage MT at the outer track of the CR is

$$v_{2m\tau w} = \omega_2(S_{c2} + r\cos\beta) \tag{11}$$

The sliding velocity between the second-stage MT and the inner track of CR2 is

$$v_{2mhn} = v_{2m\tau n} - \omega_1(S_{c2} - r\cos\beta)\cos(\varphi_{2i} - \alpha_2) \tag{12}$$

The sliding velocity between the second-stage MT and the outer track of CR2 is

$$v_{2mhw} = v_{2m\tau w} - \omega_1(S_{c2} + r\cos\beta)\cos(\varphi_{2i} - \alpha_2) \tag{13}$$

where $S_{c2} = a_2\cos Z_{K2}\varphi_{2i} + \sqrt{b_2^2 - a_2^2\sin^2 Z_{K2}\varphi_{2i}}$;

$\alpha_2 = \arctan\left(-\frac{Z_{k2}\sin z_{k2}\varphi_{2i}\cos\varphi_{2i} + \sqrt{\lambda_2^2 - \sin^2 Z_{k2}\varphi_{2i}}\sin\varphi_{2i}}{z_{k2}\sin z_{k2}\varphi_{2i}\sin\varphi_{2i} - \sqrt{\lambda_2^2 - \sin^2 Z_{k2}\varphi_{2i}}\cos\varphi_{2i}}\right)$; $\lambda_2 = b_2/a_2$ and Z_{k2} is the wave number of CR2.

The velocity v_{2mg} is the relative velocity between the second-stage MT and MTF:

$$v_{2mg} = \omega_2 \cdot \frac{dS_{c2}}{d\varphi_{2i}} = -\omega_2\left(Z_{k2}a_2\sin Z_{k2}\varphi_{2i} + \frac{a_2^2 Z_{K2}\sin 2Z_{K2}\varphi_{2i}}{2\sqrt{b_2^2 - a_2^2\sin^2 Z_{K2}\varphi_{2i}}}\right) \tag{14}$$

At the outer meshing points, the velocity of the second-stage CR is

$$v_{2kw} = -\omega_3(S_{c2} + r\cos\beta) \tag{15}$$

At the inner meshing points, the velocity of the second-stage CR is

$$v_{2kn} = -\omega_3(S_{c2} - r\cos\beta) \tag{16}$$

Thus, the relative sliding velocity between the second-stage MT and the outer track of the CR is

$$v_{2mkw} = \sqrt{(v_{2kw} - v_{2m\tau w})^2 + v_{2mg}^2} \tag{17}$$

The relative sliding velocity between the second-stage MT and the inner track of the CR is

$$v_{2mkn} = \sqrt{(v_{2kn} - v_{2m\tau n})^2 + v_{2mg}^2} \tag{18}$$

The relative sliding velocity between the second-stage MT and the outer track of the WG is

$$v_{2mhw} = v_{2m\tau w} - \omega_1(S_{c2} + r\cos\beta)\cos(\varphi_{2i} - \alpha_2) \tag{19}$$

The relative sliding velocity between the second-stage MT and the inner track of the WG is

$$v_{2mhn} = v_{2m\tau n} - \omega_1(S_{c2} - r\cos\beta)\cos(\varphi_{2i} - \alpha_2) \tag{20}$$

The velocity of the MTF along its track direction is zero. The entrainment velocity of the first-stage steel balls and the MTF at their meshing point is half of the velocity of the MT in the track direction of the MTF:

$$U_{1mg} = \frac{v_{1mg}}{2} \tag{21}$$

Since the first-stage CR is fixed, the entrainment velocity of the first-stage MT and CR at the outer meshing point is half of the velocity of the MT:

$$U_{1mkw} = \frac{\sqrt{v_{1m\tau w}^2 + v_{1mg}^2}}{2} \tag{22}$$

The angle between v_{1mkn} and $v_{1m\tau n}$ is $\varphi_{2i} - \alpha_1$, so the entrainment velocity of the first-stage steel balls and WG at the inner meshing point is:

$$U_{1mhn} = \frac{v_{1mkw} + v_{1m\tau w}\cos(\varphi_{2i} - \alpha_1)}{2} \tag{23}$$

In the same way, the entrainment velocity of the second-stage steel balls and the MTF at the meshing point is

$$U_{2mg} = \frac{v_{2mg}}{2} \tag{24}$$

Since the second CR is rotating, the entrainment velocity of the second-stage steel balls and CR at the outer meshing point is:

$$U_{2mkw} = \frac{v_{2mw}\cos(\varphi_{2i} - \alpha_2) + v_{2kw}}{2} \tag{25}$$

The entrainment velocity of the second-stage steel balls and WG at the inner meshing point is:

$$U_{2mkn} = \frac{v_{2mn}\cos(\varphi_{2i} - \alpha_2) + v_{2kn}}{2} \tag{26}$$

2.3. Forces and Friction Coefficients on Meshing Pairs

Given a WG eccentricity error, the forces on the movable tooth i can be calculated as [22]:

$$F_{1i} = \frac{F_{ji} + F_{jip}}{\sin\beta} \tag{27}$$

$$F_{2\mathrm{i}} = F_{\mathrm{si}} + F_{\mathrm{sip}} \tag{28}$$

$$F_{3i} = \frac{F_{gi} + F_{gip}}{\sin\beta} \tag{29}$$

where $F_{1\mathrm{i}}$, $F_{2\mathrm{i}}$, and $F_{3\mathrm{i}}$ are, respectively, the total force on MT1 from WG1, MTF1, and CR1; F_{ji}, F_{si}, and F_{gi} are, respectively, the force on MT1 from WG1, MTF1, and CR1 without eccentric error; and F_{jip}, F_{sip}, and F_{gip} are, respectively, the force on MT1 from WG1, MTF1, and CR1 caused by the eccentric error.

The forces on MT1 from WG1, MTF1, and CR1 without eccentric error are

$$F_{\mathrm{ji}} = \frac{(T_{A1} - T_p)\lambda_1}{Z_{t1}}(\cos Z_{\mathrm{K1}}\varphi_{2\mathrm{i}} + \sqrt{\lambda_1^2 - \sin^2 Z_{\mathrm{K1}}\varphi_{2\mathrm{i}}})\sin Z_{\mathrm{K1}}\varphi_{2\mathrm{i}} \tag{30}$$

$$F_{\mathrm{si}} = \frac{(T_{A1} - T_p)\mathrm{i}_1}{Z_{t1}}(\cos Z_{\mathrm{K1}}\varphi_{2\mathrm{i}} + \sqrt{\lambda_1^2 - \sin^2 Z_{\mathrm{K1}}\varphi_{2\mathrm{i}}})\sin^2 Z_{\mathrm{K1}}\varphi_{2\mathrm{i}} \tag{31}$$

$$F_{\mathrm{gi}} = \frac{(T_{A1} - T_p)}{Z_{t1}}(\cos Z_{\mathrm{K1}}\varphi_{2\mathrm{i}} + \sqrt{\lambda_1^2 - \sin^2 Z_{\mathrm{K1}}\varphi_{2\mathrm{i}}})\sqrt{\left(Z_{\mathrm{K1}}^2 - 1\right)\sin Z_{\mathrm{K1}}\varphi_{2\mathrm{i}} + \lambda_1^2}\sin Z_{\mathrm{K1}}\varphi_{2\mathrm{i}} \quad (32)$$

The forces on MT1 from WG1, MTF1, and CR1 caused by the eccentric error are

$$F_{jip} = E\sqrt{r\left(\frac{\Delta a}{1.231}\right)^3}\sin\theta \quad (33)$$

$$F_{\mathrm{sip}} = \frac{i_1}{\lambda_1} sin Z_{\mathrm{K1}}\varphi_{2\mathrm{i}} F_{\mathrm{jip}} = \frac{E i_1 sin Z_{\mathrm{K1}}\varphi_{2\mathrm{i}} sin\theta}{\lambda_1}\sqrt{r(\frac{\Delta a}{1.231})^3} \quad (34)$$

$$F_{gip} = \frac{E\sqrt{\left[(Z_{K1}^2 - 1)\sin Z_{K1}\varphi_{2i} + \lambda_1^2\right] r\left(\frac{\Delta a}{1.231}\right)^3}}{\lambda_1}\sin\theta \quad (35)$$

where $T_{\mathrm{A1}} = T_{\mathrm{A1zp}} + T_{\mathrm{A1xp}} + T_{\mathrm{A1sp}}$; $T_{A1zp} = (F_{ji} + F_{jip})S_{c1}\sin\gamma_1$, $T_{A1sp} = \sum_{i=2}^{n_{1z}}(F_{ji} + F_{jip})S_{c1s}\sin\gamma_1$ and $T_{A1xp} = \sum_{i=n_{1z}}^{n1}(F_{ji} + F_{jip})S_{c1x}\sin\gamma_1$; E is the elastic modulus;

$T_{\mathrm{p}} = \frac{E}{\lambda_1}\sqrt{r\left(\frac{\Delta a}{1.231}\right)^3}(S_{C1}\sin\theta\sin Z_{K1}\varphi_{2i} + \sum_{i=2}^{n_{1z}} S_{C1s}\sin\theta\sin Z_{K1}\varphi_{2i}S_{c1x} + \sum_{i=n_{1z}}^{Z_{G1}}\sum_{i=2}^{n_{1z}} S_{C1x}\sin\theta\sin Z_{K1}\varphi_{2i})$; $\mathrm{n_{1z}} = \frac{Z_{G1}-1}{2}$;

$S_{\mathrm{c1s}} = a_1\cos Z_{\mathrm{K1}}\varphi_{2\mathrm{i}} + \sqrt{(b_1 - r\cos\beta)^2 - a_1^2\sin^2 Z_{\mathrm{K1}}\varphi_{2\mathrm{i}}}$; $S_{\mathrm{c1x}} = a_1\cos Z_{\mathrm{K1}}\varphi_{2\mathrm{i}} + \sqrt{(b_1 + r\cos\beta)^2 - a_1^2\sin^2 Z_{\mathrm{K1}}\varphi_{2\mathrm{i}}}$;

$Z_{\mathrm{t1}} = Z_{\mathrm{t1z}} + Z_{\mathrm{t1s}} + Z_{\mathrm{t1x}}$; $Z_{\mathrm{t1z}} = \left(\cos Z_{\mathrm{K1}}\varphi_{2\mathrm{i}} + \sqrt{\lambda_1^2 - \sin^2 Z_{\mathrm{K1}}\varphi_{2\mathrm{i}}}\right)\sin^2 Z_{\mathrm{K1}}\varphi_{2\mathrm{i}}S_{\mathrm{c1}}$; $Z_{\mathrm{t1s}} = \sum_{\mathrm{i=2}}^{\mathrm{n_{1z}}}\left(\cos Z_{\mathrm{K1}}\varphi_{2\mathrm{i}} + \sqrt{\lambda_1^2 - \sin^2 Z_{\mathrm{K1}}\varphi_{2\mathrm{i}}}\right)\sin^2 Z_{\mathrm{K1}}\varphi_{2\mathrm{i}}(S_{\mathrm{c1}} - r\cos\beta)$; $Z_{\mathrm{t1x}} = \sum_{\mathrm{i=n_{1z}}}^{\mathrm{n1}}\left(\cos Z_{\mathrm{K1}}\varphi_{2\mathrm{i}} + \sqrt{\lambda_1^2 - \sin^2 Z_{\mathrm{K1}}\varphi_{2\mathrm{i}}}\right)\sin^2 Z_{\mathrm{K1}}\varphi_{2\mathrm{i}}(S_{\mathrm{c1}} + r\cos\beta)$.

In the same manner, the forces on the movable tooth j in the second-stage drive with eccentric error can also be given by

$$F_{1\mathrm{j}} = \frac{F_{\mathrm{jj}} + F_{\mathrm{jjp}}}{\sin\beta} \quad (36)$$

$$F_{2\mathrm{j}} = F_{\mathrm{sj}} + F_{\mathrm{sjp}} \quad (37)$$

$$F_{3\mathrm{j}} = \frac{F_{\mathrm{gj}} + F_{\mathrm{gjp}}}{\sin\beta} \quad (38)$$

where $F_{1\mathrm{j}}$, $F_{2\mathrm{j}}$, and $F_{3\mathrm{j}}$ are, respectively, the total force on MT2 from WG2, MTF2, and CR2; F_{jj}, F_{sj}, and F_{gj} are, respectively, the force on MT2 from WG2, MTF2, and CR2 without eccentric error; F_{jjp}, F_{sjp}, and F_{gjp} are, respectively, the force on MT2 from WG2, MTF2, and CR2 caused by the eccentric error.

From Figure 2e, it can be seen that the length of the contact line between the first-stage MT and CR or WG is given by

$$l_{ni} = r\sin(\frac{\pi}{2} - \gamma_{ni}) \quad (39)$$

where $\gamma_{ni} = \arcsin(\frac{a_1}{b_1}\sin(Z_{k1}\varphi_{2i}))$, n is equal to 1 for MT and CR and 2 for MT and WG.

Substituting the equation for γ_{ni} into Equation (39) ($l_{ni} = r\sqrt{1 - \frac{a_1^2}{b_1^2}\sin^2(Z_{k1}\varphi_{2i})}$) yields

$$l_{ni} = r\sqrt{1 - \frac{a_1^2}{b_1^2}\sin^2(Z_{k1}\varphi_{2i})} \tag{40}$$

Thus, the load per unit length between the first-stage MT and CR or WG is

$$W_{ni} = \frac{F_{ni}}{l_{ni}} = \frac{F_{ni}b_i}{r\sqrt{b_i^2 - a_i^2\sin^2(Z_{Ki}\varphi_{2i})}} \tag{41}$$

For the second-stage drive, Z_{ki} is replaced by Z_{k2}, φ_{2i} is replaced by φ_{2j}, b_i is replaced by b_2, and a_i is replaced by a_2 in Equation (41), so that the load W_{nj} per unit length between the second-stage MT and CR or WG can be given.

The Benedict and Kelley friction-coefficient formula is [23]

$$f_s = 0.0127\lg\left|\frac{29.66 \times 10^9 W_{ni}}{v\eta_0 U^2}\right| \tag{42}$$

where η_0 is the kinematic viscosity of the lubricant (Pa.s), U is the entrainment velocity (m/s), v is the relative velocity (m/s), and W_{ni} is the force per unit length (N/m).

Substituting Equation (41) into Equation (42) yields

$$f_s = 0.0127\lg\left|\frac{1.483 \times 10^{12} F_{ni}b_i}{v_0 U^2 r\sqrt{b_i^2 - a_i^2\sin^2(Z_{ki}\varphi_{2i})}}\right| \tag{43}$$

For the first-stage drive, Z_{ki} is taken to be Z_{k1}, φ_{2i} is taken to be φ_{2i}, b_i is taken to be b_1, and a_i is taken to be a_1. When $F_{ni} = F_{1i}$, $U = U_{1mhn}$, and $v = v_{1mhn}$, the friction coefficient f_{1mhn} between the first-stage MT and the inner surface of the WG can be determined. When $F_{ni} = F_{1i}$, $U = U_{1mhw}$, and $v = v_{1mhw}$, and the friction coefficient f_{1mhw} between the first-stage MT and outer the surface of the WG can be determined. When $F_{ni} = F_{2i}$, $U = U_{1mkn}$, and $v = v_{1mkn}$, the friction coefficient f_{1mkn} between the first-stage MT and the inner surface of the CR can be determined. When $F_{ni} = F_{2i}$, $U = U_{1mkw}$, and $v = v_{1mkw}$, the friction coefficient f_{1mkw} between the first-stage MT and outer surface of the CR can be determined.

For the second-stage drive, Z_{ki} is equal to Z_{k2}, φ_{2i} is equal to φ_{2j}, b_i is equal to b_2, and a_i is equal to a_2. When $F_{ni} = F_{1j}$, $U = U_{2mhn}$, and $v = v_{2mhn}$, the friction coefficient f_{2mhn} between the second-stage MT and the inner surface of the WG can be determined. When $F_{ni} = F_{1j}$, $U = U_{2mhw}$, and $v = v_{2mhw}$, the friction coefficient f_{2mhw} between the second-stage MT and the outer surface of the WG can be determined.

When $F_{ni} = F_{2j}$, $U = U_{2mkn}$, and $v = v_{2mkn}$, the friction coefficient f_{2mkn} between the second-stage MT and the inner surface of the CR can be determined. When $F_{ni} = F_{2j}$, $U = U_{2mkw}$, and $v = v_{2mkw}$, the friction coefficient f_{2mkw} between the second-stage MT and outer surface of the CR can be determined.

2.4. Oil Film Thickness

Meshing points of the first-stage MT and CR or WG are shown in Figure 3, which reveals the following:

Ball 1 meshes with the outer surface of the central wheel in convex–concave contact, and meshes with the inner surface of the central wheel in convex–convex contact. Ball 2 meshes with the outer surface of the central wheel in convex–convex contact, and with the inner surface of the central wheel in convex–concave contact. This means that between the movable teeth and the outer surface or the inner surface of the central wheel, convex–

convex contact occurs at some position and convex–concave contact occurs at another position. They change periodically.

The ball always meshes with the outer surface of the WG in convex–concave contact and always meshes with its inner surface in convex–convex contact.

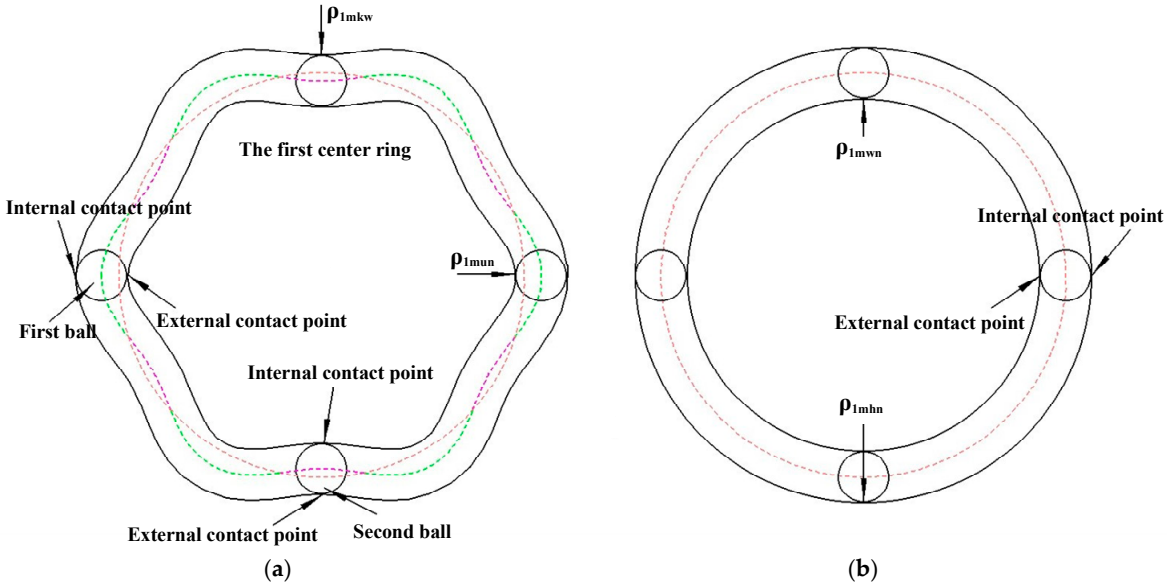


Figure 3. Meshing points and effective radius of curvature between the first-stage MT and CR or WG: (**a**) MT and CR; and (**b**) MT and WG.

When $S_{c1} < b_1$—i.e., when $\frac{(1+k)\pi}{2Z_{K1}} < \varphi_{2i} < \frac{(3+k)\pi}{2Z_{K1}} (k = 0, 1, 2, 3 \ldots)$—the ball meshes with the outer surface of the CR in convex–convex contact. So, the inverse of the effective radius of curvature is

$$\frac{1}{\rho_{1mkw}} = \frac{1}{\rho_{1k} + r\cos\beta} + \frac{1}{\rho_1} \tag{44}$$

When $S_{c1} > b_1$—i.e., when $\frac{(k-1)\pi}{2Z_{K1}} < \varphi_{2i} < \frac{(k+1)\pi}{2Z_{K1}} (k = 0, 1, 2, 3 \ldots)$—the ball meshes with the outer surface of the CR in convex–convex contact as well. So, the inverse of the effective radius of curvature is

$$\frac{1}{\rho_{1mkw}} = \frac{1}{\rho_1} - \frac{1}{\rho_{1k} + r\cos\beta} \tag{45}$$

where $\rho_{1k} = \frac{a_1\left(cosZ_{K1}\theta_1 + \sqrt{\lambda_1^2 - sin^2 Z_{K1}\theta_1}\right)\left\{\left[{Z_{K1}}^2 - 1\right]sin^2 Z_{K1}\theta_1 + \lambda_1^2\right\}^{3/2}}{{Z_{K1}}^2\lambda_1^2 cosZ_{K1}\theta_1 + \sqrt{\lambda_1^2 - sin^2 Z_{K1}\theta_1}\left\{\left[{Z_{K1}}^2 - 1\right]sin^2 Z_{K1}\theta_1 + \lambda_1^2\right\}}$ is the radius of curvature for the tooth centered on the first-stage CR. $\rho_1 = r_1\cos\beta$, r_1 is the first-stage MT radius.

When $S_{c1} < b_1$—i.e., when $\frac{(1+k)\pi}{2Z_{K1}} < \varphi_{2i} < \frac{(3+k)\pi}{2Z_{K1}} (k = 0, 1, 2, 3 \ldots)$—the ball meshes with the inner surface of the CR in convex–concave contact. So, the inverse of the effective radius of curvature is

$$\frac{1}{\rho_{1mkn}} = \frac{1}{\rho_1} - \frac{1}{\rho_{1k} - r\cos\beta} \tag{46}$$

When $S_{c1} > b_1$¯i.e., when $\frac{(k-1)\pi}{2Z_{K1}} < \varphi_{2i} < \frac{(k+1)\pi}{2Z_{K1}} (k = 0, 1, 2, 3 \ldots)$—the ball meshes with the inner surface of the CR in convex–convex contact. So, the inverse of the effective radius of curvature is

$$\frac{1}{\rho_{1mkn}} = \frac{1}{\rho_1} + \frac{1}{\rho_{1k} - r\cos\beta} \tag{47}$$

When the ball meshes with the outer surface of the WG in convex–concave contact, the effective radius of curvature is

$$\rho_{1mhw} = \frac{r(b_1 + r\cos\beta)}{b_1 + r\cos\beta - r} \tag{48}$$

When the ball meshes with the inner surface of the WG in convex–convex contact, the effective radius of curvature is

$$\rho_{1mhn} = \frac{r(b_1 - r\cos\beta)}{b_1 - r\cos\beta + r} \tag{49}$$

In the same way, the effective radius of curvature for the second-stage drive can be found as follows:

When the ball meshes with the outer surface of the CR in convex–convex contact, the effective radius of curvature is

$$\rho_{2mkw} = \frac{r(\rho_{2k} + r\cos\beta)}{\rho_1\left(\frac{S_{c2}-b_2}{|S_{c2}-b_2|}\right) + (\rho_{2k} + r\cos\beta)} \tag{50}$$

When the ball meshes with the inner surface of the CR in convex–convex contact, the effective radius of curvature is

$$\rho_{2mkn} = \frac{r(\rho_{2k} - r\cos\beta)}{\rho_1\left(\frac{S_{c2}-b_2}{|S_{c2}-b_2|}\right) + (\rho_{2k} - r\cos\beta)} \tag{51}$$

When the ball meshes with the outer surface of the WG, the effective radius of curvature is

$$\rho_{2mhw} = \frac{r(b_2 + r\cos\beta)}{b_2 + r\cos\beta - r} \tag{52}$$

When the ball meshes with the inner surface of the WG, the effective radius of curvature is

$$\rho_{2mhn} = \frac{r(b_2 - r\cos\beta)}{b_2 - r\cos\beta + r} \tag{53}$$

The minimum oil film thickness (MOFT) for the meshing pairs can be given by [24]

$$H_{\min} = 2.65\frac{\alpha^{0.54}(\eta_0 \cdot U)^{0.7}\rho^{0.43}}{E'^{0.03}W_{ni}{}^{0.13}} \tag{54}$$

where α is the pressure–viscosity coefficient (m^2/N), η_0 is the dynamic viscosity of the lubricating oil (Pa·s), U is the entrainment velocity (m/s), ρ is the equivalent curvature radius (m), E' is the effective elastic modulus (Pa), and W_{ni} is the force per unit length (N/m).

Substituting related equations into Equation (54) yields

$$H_{\min} = \frac{2.65\alpha^{0.54}(\eta_0)^{0.7}U^{0.7}\rho^{0.43}\left(r\sqrt{1 - \frac{a_i^2}{b_i^2}\sin^2(Z_{ki}\varphi_{2i})}\right)^{0.13}}{F_{ni}^{0.13}} \tag{55}$$

(here, α is taken to be $2.1 \times 10^{-8} m^2/N$).

For the first-stage drive, Z_{ki} is taken to be Z_{k1}, φ_{2i} is taken to be φ_{2i}, b_i is taken to be b_1, and a_i is taken to be a_1. When $F_{nic} = F_{1i}$, $U = U_{1mhn}$, and $\rho = \rho_{1mhn}$, the MOFT H_{1mhn} between the first-stage MT and the inner surface of the WG can be determined. When $F_{ni} = F_{1i}$, $U = U_{1mhw}$, and $\rho = \rho_{1mhw}$, the MOFT H_{1mhw} between the first-stage MT and the

outer surface of the WG can be determined. When $F_{ni} = F_{2i}$, $U = U_{1mkn}$, and $\rho = \rho_{1mkn}$, the MOFT H_{1mkn} between the first-stage MT and the inner surface of the CW can be determined. When $F_{ni} = F_{2i}$, $U = U_{1mkw}$, and $\rho = \rho_{1mkw}$, the MOFT H_{1mkw} between the first-stage MT and the outer surface of the CW can be determined.

For the second-stage drive, $Z_{ki} = Z_{k2}$, $\varphi_{2i} = \varphi_{2j}$, $b_i = b_2$, and $a_i = a_2$. When $F_{ni} = F_{1j}$, $U = U_{2mhn}$, and $\rho = \rho_{2mhn}$, the MOFT H_{2mhn} between the second-stage MT and the inner surface of the WG can be determined. When $F_{ni} = F_{1j}$, $U = U_{2mhw}$, and $\rho = \rho_{2mhw}$, the MOFT H_{2mhw} between the second-stage MT and the outer surface of the WG can be determined. When $F_{ni} = F_{1j}$, $U = U_{2mkn}$, and $\rho = \rho_{2mkn}$, the MOFT H_{2mkn} between the second-stage MT and the inner surface of the CW can be determined. When $F_{ni} = F_{2j}$, $U = U_{2mkw}$, and $\rho = \rho_{2mkw}$, the MOFT H_{2mkw} between the second-stage MT and the outer surface of the CW can be determined.

2.5. Friction Loss and Efficiency

The efficiency of the movable tooth gear reducer is affected mainly by sliding and rolling friction loss. The sliding friction loss for one movable tooth can be calculated by

$$P_s = f_s F_{ni} v \tag{56}$$

where f_s is the sliding friction factor.

The rolling friction loss of one movable tooth can be calculated by [22]

$$P_R = 9 H_{\min} l_{ni} U \cdot 10^{-5} \tag{57}$$

where P_R is the rolling friction power loss (W), $H_{\min}$ is the minimum oil film thickness (m), lni is the length of contact line (m), and U is the entrainment velocity (m/s).

Substituting Equation (40) into Equation (57) yields

$$P_R = 9 H_{\min} r \sqrt{1 - \frac{a_i^2}{b_i^2} \sin^2(Z_{ki} \varphi_{2i})} U \cdot 10^{-5} \tag{58}$$

In Equations (56) and (58), the same parameter substitutions as used for calculating the minimum oil film thickness are made, allowing for friction power losses to be determined, as follows:

For the first-stage drive, friction losses are P_{s1mhn} (sliding) and P_{r1mhn} (rolling) between the first-stage MT and the inner surface of the WG, P_{s1mhw} (sliding) and P_{r1mhw} (rolling) between the first-stage MT and the outer surface of the WG, P_{s1mkn} (sliding) and P_{r1mkn} (rolling) between the first-stage MT and the inner surface of the CW, and P_{s1mkw} (sliding) and P_{r1mkw} (rolling) between the first-stage MT and the outer surface of the CW.

For the second-stage drive, friction losses are P_{s2mhn} (sliding) and P_{r2mhn} (rolling) between the second-stage MT and the inner surface of the WG, P_{s2mhw} (sliding) and P_{r2mhw} (rolling) between the second-stage MT and the outer surface of the WG, P_{s2mkn} (sliding) and P_{21mkn} (rolling) between the second-stage MT and the inner surface of the CW, and P_{s2mkw} (sliding) and P_{r2mkw} (rolling) between the second-stage MT and the outer surface of the CW.

When there are $2n$ balls (movable teeth) in the i-th-stage movable tooth drive, its total power loss is

$$P_m = \sum_{i=1}^{n} P_{in} + \sum_{i=n}^{2n} P_{iw} \tag{59}$$

where m is 1 for the first-stage drive and 2 for the second-stage drive; P_{in} denotes power loss on the inner surfaces; and P_{iw} denotes power loss on the outer surfaces.

Thus, the total power loss is

$$P = P_1 + P_2 \tag{60}$$

Therefore, the meshing efficiency for the reducer is

$$\eta_m = \frac{T_{em} \cdot \omega_1 - P}{T_{em} \cdot \omega_1} \times 100\% \tag{61}$$

where T_{em} is the input torque from the motor and ω_1 is the angular speed of the motor (equal to the angular speed of the first WG).

3. Results

Using the above equations, the relative sliding velocities in the reducer are calculated when the load is applied to the inner and outer tracks (see Figure 4). Table 1 gives the calculated parameters for the reducer. The motor speed is 210 rpm. Firstly, the ratios $\lambda_1 = b_1/a_1$ and $\lambda_2 = b_2/a_2$ were calculated according to the parameters in Table 1, and the angular speeds ω_1, ω_2, and ω_3 are calculated according to motor input speeds and transmission ratios. Then, substituting them into the equations of the central distance S_{c1} and S_{c2}, the angle α_1 and α_2, and the relative sliding velocities, the relative sliding speed of the reducer with the change of the rotation angle can be obtained. Here are some results:

(1) In the closed reducer, the relative velocity between the MT and the MT frame is very small, it is sinusoidal, and it is not affected by changes of the inner or outer surfaces of the WG.
(2) The relative velocity for the MT and the WG is opposite to that of the MT and the CW. The former is greater than the latter, and both are much greater than the relative speed of the MT and the MT frame.
(3) When the MT meshes with the inner surface of the WG, the relative velocity between them is the greatest, and the velocity fluctuations are also the greatest. When the MT meshes with the outer surface of the WG, both the relative velocity and the velocity fluctuations are maximum. When the MT meshes with the outer surface of the WG, both the relative velocity and its fluctuations are larger than when the MT meshes with the inner surface of the WG.
(4) When the MT meshes with the inner surface of the CW, both relative velocity and its fluctuations are larger than when the MT meshes with the outer surface of the WG.
(5) A large sliding velocity can cause a large friction loss between meshing pairs. The results above show that the friction power loss between the MT and the WG could be at a maximum while the friction power loss between the MT and the MT frame is at a minimum. The meshing efficiency of the reducer could depend on the friction power loss between the MT and the WG or the CW. Among these, the effects of the friction power loss between the MT and the WG on the efficiency could be most significant.

Using the above equations, the entrainment velocities between meshing pairs are calculated when the load is applied to the inner and outer tracks (see Figure 5). Here are some results:

(1) In a two-stage drive, the entrainment velocity of the MT and the MT frame is very small, and it is also sinusoidal and not affected by changes of the inner or outer surfaces of the WG.
(2) When the first-stage MT meshes with the inner track of the WG, the entrainment velocity between them is close to the entrainment velocity between the MT and the CW. Under other conditions, the entrainment velocities between the MT and the WG are much greater than those between the MT and the CW.

(3) For the first-stage drive, when the MT meshes with the outer surface of the WG, the entrainment velocity between them is larger than when the MT meshes with the inter surface of the WG. When the MT meshes with the outer surface of the CW, the entrainment velocity between them is larger than that when the MT meshes with the inner surface of the CW.

(4) When the second-stage MT meshes with the outer surface of the WG, the entrainment velocity between them is larger than that when the MT meshes with the inner surface of the WG. When the MT meshes with the outer surface of the CW, the entrainment velocity between them is smaller than that when the MT meshes with the inner surface of the CW.

(5) Both sliding and rolling friction coefficients are affected by the entrainment velocity between meshing pairs. The increase of the entrainment velocity could lead to the increase of the rolling friction coefficient and an evident decrease of the sliding friction coefficient, which causes increasing rolling-friction power loss and concurrently a decrease in the sliding-friction power loss. Thus, the meshing efficiency can be increased.

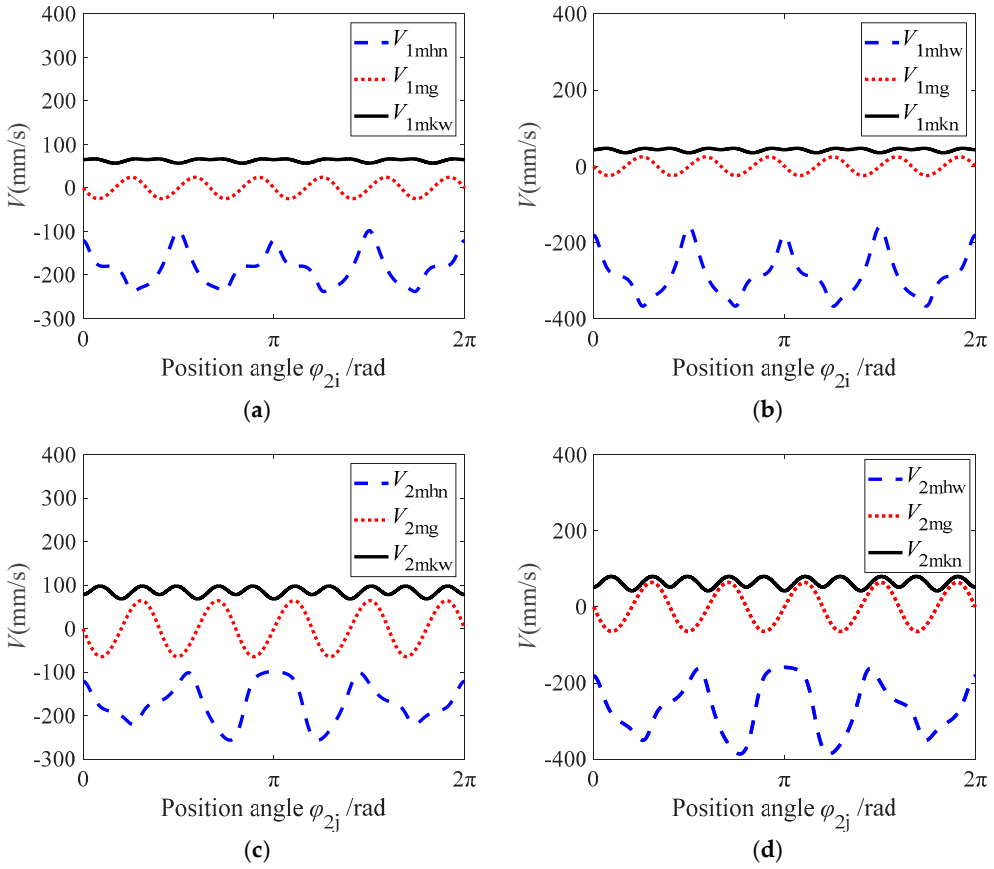


Figure 4. Relative sliding velocities: (**a**) inner track of the first wave generator; (**b**) outer track of the first wave generator; (**c**) inner track of the second wave generator; and (**d**) outer track of the second wave generator.

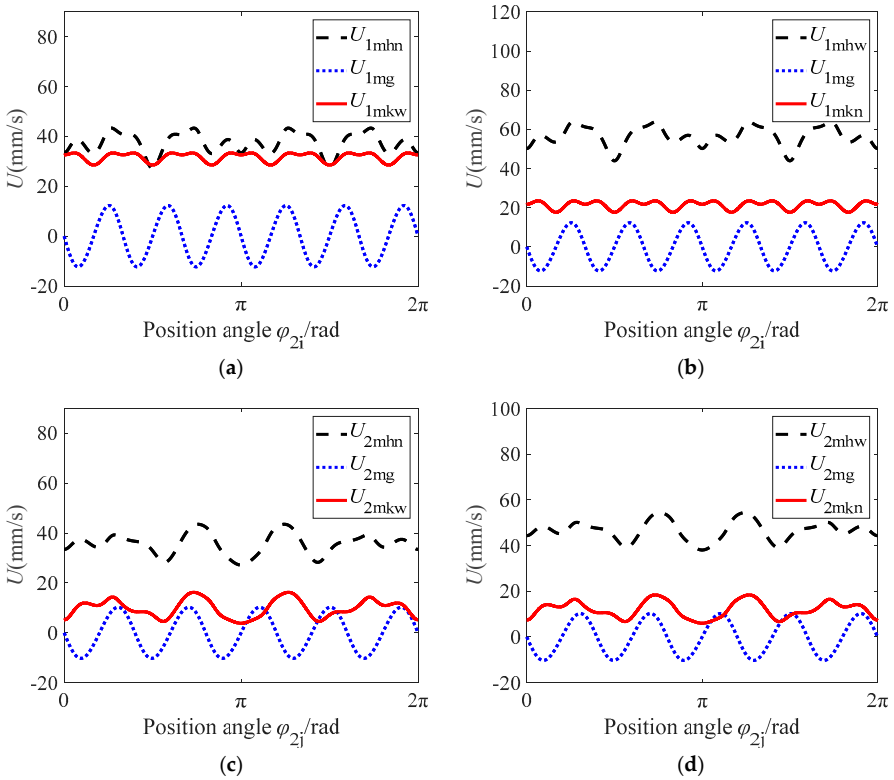


Figure 5. Entrainment velocities between meshing pairs: (**a**) inner track of the first wave generator; (**b**) outer track of the first wave generator; (**c**) inner track of the second wave generator; and (**d**) outer track of the second wave generator.

By substituting the related parameters into the equations of the effective curvature radius of the meshing pair, the changes of the effective curvature radius r with angular position can be obtained. The motor torque T_{em} is taken to be 0.14 N m. The steel balls are made of bearing steel (Gr15), and the center wheel, wave generator, and movable tooth frame are made of alloy steel (42CrMo). The material parameter required for calculation is elastic modulus (E = 210 GPa). Given the eccentricity error Δa of WG, the force distribution of meshing pair for the reducer can be obtained by substituting the related parameters into the force equations. The pressure–viscosity coefficient of the lubricant oil α is taken to be 2.1×10^{-8} m^2/N, and $\eta_0 = 2 \times 10^{-8}$ MPa·s. The minimum oil film thickness of the meshing pair can be determined by substituting the two parameters together with the formula of the effective curvature radius and the force into the minimum oil film thickness equation. The power loss of the meshing pair can be determined by substituting the minimum oil film thickness and related parameters into the power loss formula. Then, the power loss plus input torque T_{em} and angular speed ω_1 of the motor is substituted into the efficiency equation, and the meshing efficiency of the reducer can be determined. Figure 6 shows the effects of changes in reducer size parameters on transmission efficiency. Here are some results:

(1) The meshing efficiency of the reducer changes periodically with the angular position, which is caused by the periodic change of the friction coefficient between the tooth surfaces and the effective radius of curvature.

(2) With increasing eccentric distance for the first and second drives, the meshing efficiency of the reducer is increased. This is because increasing the eccentric distance reduces the pressure angle between meshing pairs so that the effective driving force is increased. When an error in the eccentric distance occurs, the meshing efficiency

of the reducer is decreased significantly. This is because the error of the eccentric distance causes an obvious increase in the friction power loss between meshing pairs.

(3) When the radius b_1 or b_2 is decreased, the meshing efficiency of the first and the second drives of the reducer is decreased slightly. This is because a decrease of b_1 or b_2 reduces the effective radius of curvature between meshing pairs, and the oil film thickness is reduced so that friction power loss is increased.

(4) When angle β_1 or β_2 is increased, the meshing efficiency of the first and the second drives of the reducer is decreased. This is because increasing the angle β_1 or β_2 causes axial forces between meshing pairs to be increased so that the effective driving forces in the operation plane are reduced.

(5) When the radius r_1 or r_2 of the movable teeth increases, the meshing efficiency of the first and the second drives of the reducer is increased slightly. This is because an increase in the radius r_1 or r_2 increases the effective radius of curvature between meshing pairs; the oil film thickness is increased so that friction power loss is decreased.

For different input speeds, the meshing efficiency as a function of the load torque is calculated. Figure 7 shows the calculation results of the change of transmission efficiency with the speed and torque under fixed size parameters. Several things can be concluded:

At a given speed, as the load torque increases, the meshing efficiency of the reducer increases, reaching a maximum value at some torque, and then decreasing gradually.

When the input speed is increased, the meshing efficiency is increased, and the load torque corresponding to the maximum meshing efficiency also increases significantly.

When the input speed increases from 143 rpm to 181 rpm, the maximum meshing efficiency is increased from 57% to 66.5%.

The efficiency of a reducer is not only related to transmission parameters, but also to speed and torque. When other parameters are constant, the efficiency gradually increases with the increase of torque, and then decreases after reaching the maximum value. The input torque in Figure 6 is T_{em} = 0.14 N m, corresponding to the load torque 2 Nm. So, the efficiency is relatively low, which is basically consistent with the efficiency value corresponding to T_{c} = 2 Nm in Figure 7.

To verify the calculated results presented in this paper, a reducer prototype was fabricated and an efficiency experiment was carried out. The experimental platform is shown in Figure 8a.

On the experimental platform, the load output torque T_{c} of the reducer is loaded by a magnetic loader. The load torque and input torque of the reducer are measured with two torque sensors. Measured operation efficiency can be determined by

$$\eta = \frac{T_c}{T_{em} \times i} \times 100\% \tag{62}$$

Here, i = 35 and input speed n_1 = 180 rpm.

Measured operation efficiency is given in Figure 8c, showing the changes of the operation efficiency along with load torque under fixed size parameters. The dimensions of the proposed reducer for calculation and the prototype reducer are the same (the dimensions of the reducers in Figures 7 and 8 are the same). The measured maximum efficiency is 63% and the calculated maximum efficiency at 180 rpm is 66.5%. They are in reasonable agreement. The difference between them is caused by friction power loss of the bearings.

Figure 8c also shows that changes of the operation efficiency along with load torque are consistent with the calculated ones in Figure 7. The difference between the two is that Figure 7 does not consider bearing friction loss and oil stirring loss. At light loads, bearing friction loss and oil stirring loss have a relatively significant impact on the overall transmission efficiency of the reducer. As the load increases, the proportion of bearing

friction loss and oil stirring loss decreases, and the impact on the overall transmission efficiency of the reducer becomes relatively smaller. Therefore, when the torque is 4 Nm, there is a significant difference between the results in Figures 7 and 8a. At 7 Nm, the results in Figures 7 and 8a are closer.

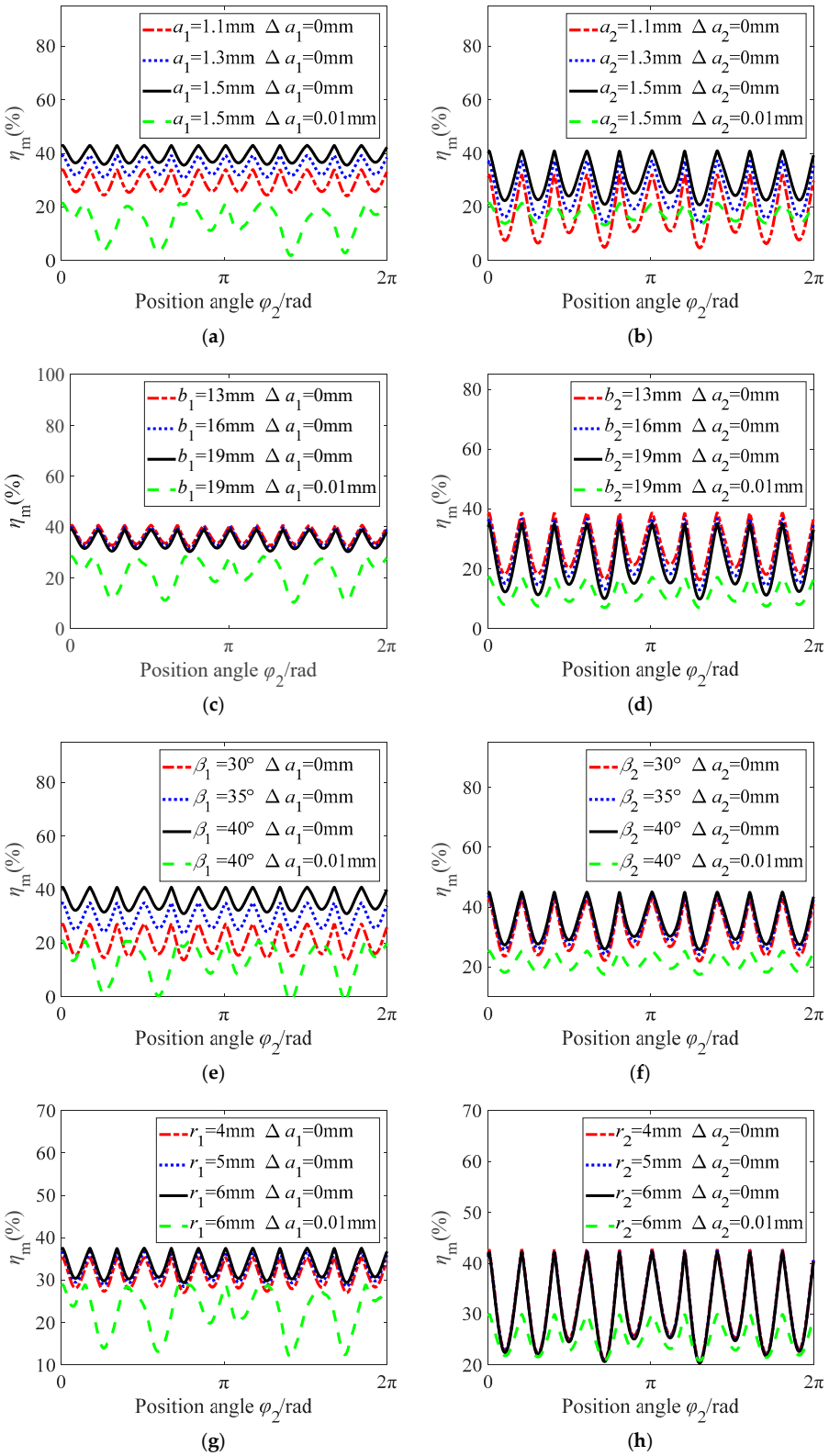


Figure 6. Meshing efficiency as function of the main parameters: (**a**) a_1 changes; (**b**) a_2 changes; (**c**) b_1 changes; (**d**) b_2 changes; (**e**) β_1 changes; (**f**) β_2 changes; (**g**) r_1 changes; and (**h**) r_2 changes.

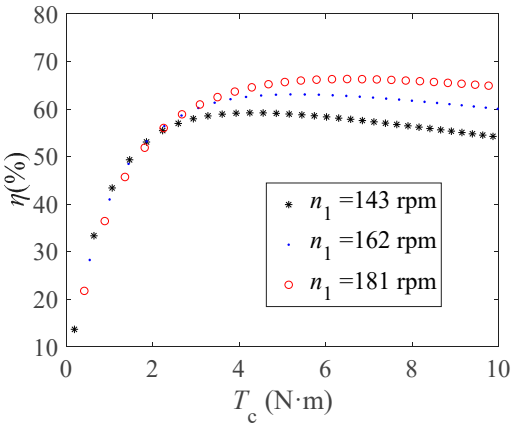
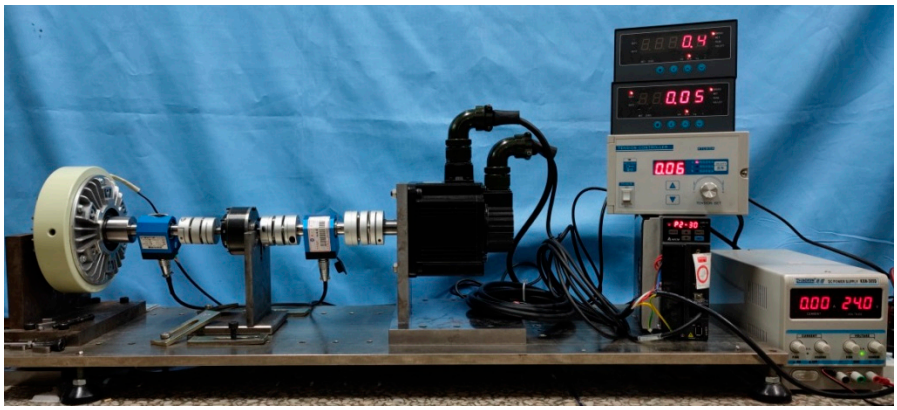
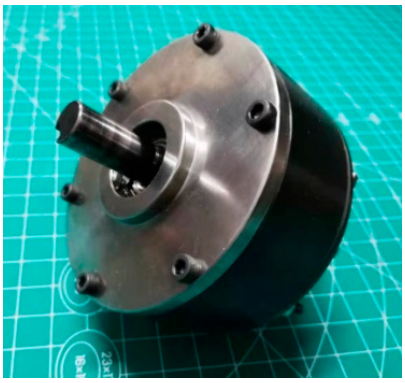


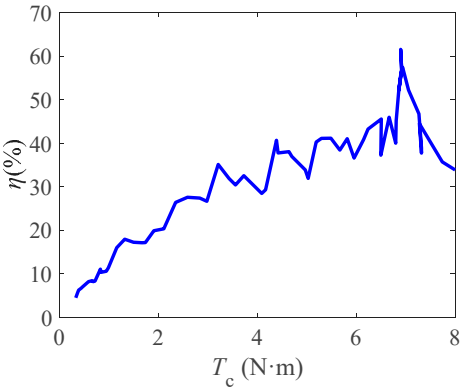
Figure 7. Meshing efficiency as a function of load torque.



(**a**)



(**b**)



(**c**)

Figure 8. Efficiency experiment and model machine: (**a**) efficiency experimental platform; (**b**) model machine; and (**c**) efficiency–load torque relation.

4. Discussion

In reference [25], the transmission efficiencies of the traditional planar ball reducer and a new eccentric driven planar ball reducer are measured and compared. The measured efficiency of the traditional planar ball reducer is 41.5%, while the transmission efficiency of the new eccentric driven planar ball reducer is 81.4%. Here, the speed ratio of the reducer model machine is 7. The outstanding characteristics of the closed-type planar movable tooth gear reducer proposed in this paper are compact structure and large speed ratio. The speed ratio of the model machine is 35, and its volume is close to that of the reducer with a speed ratio of 7 in reference [25]. The measured transmission efficiency is 63%. In order to achieve a speed ratio of 35, the reducer in reference [25] needs to adopt

a two-stage structure, and the corresponding transmission efficiency is estimated to be 81.4 × 81.4% = 66%. The efficiency is close to that of the reducer in this paper. To sum up, the reducer in this paper has a similar efficiency with the reducer proposed in reference [25] under the condition of the same speed ratio, but its volume is only about half of that in reference [25], so it has obvious advantages.

5. Conclusions

The equations of the relative sliding velocities, entrainment velocities, forces, friction coefficients, effective radius of curvature, and oil film thickness of a novel planar movable tooth gear reducer were introduced. Based on them, the equations of the friction loss and meshing efficiency for the reducer were derived. The relative sliding velocities and entrainment velocities of the reducer were studied. Meshing efficiencies and their changes, along with meshing positions and main parameters, were analyzed. Changes of the meshing efficiencies along with load torque were also studied. An efficiency experiment of the reducer prototype was carried out. The principal conclusions are the following:

(1) The relative velocity of the movable teeth and the wave generator is greater than that of the movable teeth and the central ring. Both are much greater than the relative speed of the movable teeth and the movable tooth frame. The meshing efficiency depends mainly on the friction loss between the movable teeth and the wave generator or the movable teeth and the central wheel.

(2) The entrainment velocity between the movable teeth and the inner track of the wave generator is close to the one between the movable teeth and the central wheel. Under other conditions, the entrainment velocities are much greater than those of the movable teeth and the central wheel. The increase of the entrapment velocity could lead to an increase of the rolling friction power loss and a decrease of the sliding friction power loss.

(3) The meshing efficiency changes periodically; this is caused by the periodic change of the relative sliding speed and the effective radius of curvature. With increasing eccentric distance, the meshing efficiency is increased. When an eccentric distance error occurs, the meshing efficiency is significantly reduced.

(4) When the motor speed increases, the meshing efficiency increases. The load torque corresponding to the maximum meshing efficiency also increases significantly. The measured maximum efficiency is close to the calculated maximum efficiency, supporting the theoretical studies in this paper.

Author Contributions: Conceptualization, L.X.; methodology, L.X. and S.Y.; software, S.Y.; validation, S.Y. and L.X.; formal analysis, L.X. and S.Y.; investigation, L.X. and S.Y.; writing—original draft preparation, S.Y.; writing—review and editing, L.X.; visualization, S.Y.; supervision, L.X.; project administration, L.X.; funding acquisition, L.X. All authors have read and agreed to the published version of the manuscript.

Funding: This research was funded by the National key R&D Program of China, grant number 2018YFB1304800.

Data Availability Statement: The original contributions presented in this study are included in the article Further inquiries can be directed to the corresponding author.

Conflicts of Interest: The authors declare no conflicts of interest. The funders had no role in the design of the study; in the collection, analyses, or interpretation of data; in the writing of the manuscript; or in the decision to publish the results.

References

1. Mo, S.; Zhang, Y.; Wu, Q. Load sharing characteristics of RV transmission mechanism in robot. *Mech. Mach. Sci.* **2016**, *36*, 977–987.
2. Li, Z.; Melek, W.; Clark, C. Decentralized robust control of robot manipulators with harmonic drive transmission and application to modular and reconfigurable serial arms. *Robotica* **2009**, *27*, 291–302. [CrossRef]
3. Kennedy, C.; Desai, J. Modeling and control of the Mitsubishi PA-10 robot arm harmonic drive system. *IEEE-ASME Trans. Mechatron.* **2005**, *10*, 263–274. [CrossRef]
4. Terada, H. The development of gearless reducers with rolling balls. *Korean Soc. Mech. Eng.* **2010**, *24*, 185–195. [CrossRef]
5. Vassileva, D.; Kiyosawa, Y.; Suzuki, M. Sensorless torque control for a robot with harmonic drive reducers. *Mech. Based Des. Struct. Mach.* **2011**, *39*, 253–267. [CrossRef]
6. Keith, S. Subtractive and Additive Differential Gear Reduction System. U.S. Patent US4338830A, 2 July 1982.
7. Imase, K. Ball-Rolling Type Torque Transmission Device. U.S. Patent US5683323A, 4 November 1997.
8. Terada, H.; Makino, H.; Imase, K. Fundamental analysis of cycloid ball reducer (3rd Report)—Strength Design. *JSPE* **1995**, *12*, 1705–1709.
9. Sapsalev, A.V. Comparison of the linear tachograms of cyclic gearless electric drives. *Vestn Mashinostr* **2004**, *3*, 12–15.
10. Sapsalev, A.V. Optimizing cyclic gearless electric drives with a reduced-speed section. *Russ. Eng. Res.* **2012**, *32*, 438–443. [CrossRef]
11. Terada, H.; Imase, K. Fundamental analysis of a cycloid ball reducer (5th Report)—Development of a two stage type reduction mechanism. *JSPE* **2009**, *12*, 1418–1422.
12. Yang, R.; Li, F.; Zhou, Y. Nonlinear dynamic analysis of a cycloidal ball planetary transmission considering tooth undercutting. *Mech. Mach. Theory* **2020**, *145*, 103694. [CrossRef]
13. Nam, W.; Shin, J.; Oh, S. Design of thin plate-type speed reducers using balls for robots. *J. Mech. Sci. Technol.* **2013**, *27*, 519–524. [CrossRef]
14. Nishibe, S.; Mitsufuji, S.; Nishtani, Y. Eccentric Oscillating Reduction Gear for Joint Drive of Robot. JP Patent JP2014161952A, 16 May 2014.
15. Furuta, K. Eccentric-Oscillating Gear Device. Ger. Patent DE102016201055A1, 12 July 2016.
16. Wei, R.; Jin, H.; Yi, Y. Research on the transmission error of swing-rod movable teeth transmission system. *Mech. Ind.* **2020**, *21*, 409. [CrossRef]
17. Yi, Y.; Gao, Y.; He, L. Thermoelastic stress--strain analysis of the meshing pairs of a two-tooth difference swing-rod movable toothed drive. *Strength Mater.* **2019**, *51*, 633–645. [CrossRef]
18. Xu, L.; Wang, W. Quasi-static analysis of forces and stress for a novel two-step movable tooth drive. *Mech. Based Des. Struct. Mach.* **2018**, *46*, 285–295.
19. Li, C.; Xing, J.; Fang, J. Numerical analysis on chaotic vibration of drive system for a movable tooth piezoelectric motor. *Shock Vib.* **2017**, *2017*, 3216010. [CrossRef]
20. Liang, Y.; Xu, L. Coupled dynamics for an electromagnetic harmonic movable-tooth drive system with eccentricity. *Appl. Math. Model.* **2021**, *90*, 703–718. [CrossRef]
21. Xu, L.; Li, R. Planar two-stage movable tooth reducer closed by input shaft. *J. Adv. Mech. Des. Syst. Manuf.* **2020**, *14*, 20-00090. [CrossRef]
22. Crook, A.W. The Lubrication of Rollers IV. Measurements of Friction and Effective Viscosity. *R. Soc.* **1962**, *68*, 281–312.
23. Benedict, G.H.; Kelley, B.W. Instantaneous Coefficients of Gear Tooth Friction. *ASLE Trans.* **1961**, *4*, 59–70. [CrossRef]
24. Dowson, D.; Higgison, G.R. *Elasto-Hydrodynamic Lubrication*; Pergamon Press: London, UK, 1977.
25. Xu, L.; Yang, X. Relative velocity and meshing efficiency for a novel planar ball reducer. *Mech. Mach. Theory* **2021**, *155*, 104057. [CrossRef]

Disclaimer/Publisher's Note: The statements, opinions and data contained in all publications are solely those of the individual author(s) and contributor(s) and not of MDPI and/or the editor(s). MDPI and/or the editor(s) disclaim responsibility for any injury to people or property resulting from any ideas, methods, instructions or products referred to in the content.